Assessing Micro-Void Formation at the Tips of Fibers within the Microstructure of Additively Manufactured Polymer Composite Bead

A. Awenlimobor ^{1[0009-0000-7880-2992]}, N. Sayah ^{1[0000-0002-1906-128X]} and D.E. Smith ^{1[0000-0001-8036-0345]}

Baylor University, Waco, TX 76798, USA douglas e smith@baylor.edu

Abstract. Micro-voids within the bead microstructure of additively manufactured short carbon fiber- reinforced polymer composites are known to compromise the material performance. Unfortunately, a comprehensive understanding of the formation mechanisms of micro-voids during polymer processing is currently lacking. The present study considers micro-void nucleation at fiber interfaces, particularly those occurring at the end of suspended fibers. Microcomputed tomography (µCT) image acquisition techniques are used to characterize microstructural features of a 13wt% carbon fiber reinforced ABS composite bead manufactured via Large Area Additive Manufacturing (LAAM). The results reveal a significant collection of micro-voids at the tips of fibers approaching 80% of the total micro-void volume fraction. In addition, fiber tip micro-voids are relatively larger and less spherical than micro-voids isolated within the ABS matrix. Theoretical formulations of several known mechanisms for micro-void nucleation during LAAM material processing indicate that localized fluid pressure likely plays a pivotal role in micro-void formation. To better expose this mechanism, we simulate the hydrostatic flow-field pressure distribution surrounding a single rigid fiber suspended in simple shear flow using finite element analysis (FEA). Computed results demonstrate that the polymer matrix pressure decreases significantly at the fiber ends where micro-void nucleation is experimentally observed to occur. Our approach provides the fiber surface pressure distribution in simple shear flow that typifies nozzle regions with extreme flow conditions, enhancing our understanding of micro-void development mechanisms as the polymer melt flows through the nozzle.

Keywords: Additive Manufacturing, Voids, Microstructure, Polymer Composites, Fiber Reinforcement

1 Introduction

Polymer composites materials manufactured by LAAM technology are usually consolidated with discontinuous fibers due to their superior material properties compared to virgin polymers [1-3]. Although, there are obvious benefits resulting from carbon fiber reinforcement, optimal material behavior of manufactured composites is

limited by the inherent complexities of the uncontrolled microstructure particularly the unwanted micro-porosities and unpredictable distribution of the fiber orientation [4-7]. These micro-voids are found in literature to have highly deleterious effects on the material properties of the printed composite parts compared to inter-layer voids that exists as narrow gaps between adjacent beads and aligns along the print direction during the deposition process [8-9]. The strength of the composite materials is limited by micro-voids that nucleate at the fiber-matrix interface which pose as sites for stress intensification [8-9]. Micro-voids have been identified in various literature [10-12] to arise from numerous sources such as air entrapment within the raw pellets during the compounding/pelletization process, moisture absorption or dissolution of gases within the polymer melt during processing, and restrained volume contraction due to uneven cooling across the extrudate strand during solidification process. Other factors identified in literature [10-12] that may promote micro-voids development within polymer composite includes mismatch in the coefficient of thermal expansion between the fiber and matrix phase, the suspension rheology, the distribution of the length and orientation of fiber reinforcement within the polymer, and the die-swell/expansion at the nozzle exit upon exposure of the free extrudate to the atmosphere. Yang et al. [13] found that during polymer processing, the volume fraction of micro-voids is negligible within the extruder/nozzle, however the void content peaks when the polymer melt just exits the nozzle during die-swell and drops to a stable value upon bead deposition. Under favorable operating conditions (temperature, pressure, and extrusion rate), micro-bubbles may form within the pure polymer matrix phase or at the interface of the fiber and matrix phase. Micro-voids that form at the fiber-matrix interface may be due in part to failure of the adhesive/sizing agent that results in fiber-matrix debonding [14]. Higher micro-void contents were found to be a direct consequence of increasing fiber concentrations in the raw pellets due to an overall increase in the effective viscosity of the suspension [10,13,15]. Additionally, micro-voids have been experimentally observed to segregate at the ends of fibers in dense polymer suspension with high fiber volume fractions [8,10]. Although high fiber packing is found to reduce the potential of micro-voids nucleation at the interstices between fibers, the increased number of fiber ends are observed to provide favorable sites for void nucleation to occur [8,13]. In the theory of most known micro-void nucleation mechanisms found in numerous literatures, a necessary requirement for the instigation of stable micro-voids during polymer processing is a net drop in the instantaneous hydrostatic flow-field pressure below some reference value such as the melt vapor pressure or the atmospheric pressure [16-22]. This implies that the local pressure distribution within the polymer melt plays a pivotal role in the micro-void formation process. Simulating the surrounding fluid pressure distribution around a fiber's surface may thus be important in understanding the underlying mechanisms potentially responsible for the experimentally observed dominant heterogenous mode of micro-void nucleation at the fiber-matrix interface.

Various analytical and computational methods with differing degrees of accuracy currently exist for predicting the local flow-field of typical polymer flow processes. Perhaps the most basic model that provides a fundamental basis for studying discontinuous fiber polymer composite melt flow is the notorious Jeffery's analytical formu-

lations [23] widely used to investigate the dynamics of suspended particles in viscous Newtonian low-Reynolds number dilute suspension. Jeffery's model is however limited to non-deformable, fixed-shape ellipsoidal particles and cannot be used to model suspensions with complex fluid rheology such as non-Newtonian or visco-elastic fluid behavior. Various modelling approaches have been employed by numerous researchers to account for deviations from standard Jeffery's model assumptions. For example, Abhati et al. [24] used 3D asymptotic analysis to simulate particle kinematics in non-Newtonian simple shear flow. The finite element method (FEM) has been widely used in the literature to simulate non-standard Jeffery's condition in particle suspension. Zhang et al. [25] used a coupled FEM - Brownian dynamic simulation (BDS) to investigate Brownian effects on the particles. Ferec et al. [26] used FEM to investigate the effects of shear-thinning suspension rheology on the particle's dynamics. While polymer composite modelling in literature has mostly focused on investigating the dynamics of particle reinforcement during polymer processing, little computational effort has been made to study the development of micro-voids within print beads. Using 2D FEA simulation to predict the local flow-field pressure surrounding an ellipsoidal particle in the polymer melt suspension of a typical LAAM extrusiondeposition process, Awenlimobor et al. [27] showed that high pressure fluctuations occurred at the ends of suspended particles which are likely responsible for microvoid formation.

The advent of X-ray micro-computed tomography (μ CT) imaging technique has led to higher resolution three-dimensional (3D) visualization and more accurate characterization of the microstructure of polymer composites compared to 2D imaging techniques such as scanning electron microscopy (SEM) [5,6,28]. μ CT has been widely used to identify and characterize the microstructures of polymer composites including inherent micro-constituents' phases and defects. In existing literature, the phenomenon of micro-voids nucleation at fiber tips have only previously been addressed from a qualitative perspective [10-11].

In this article, we investigate the phenomenon of micro-void nucleation at the fiber/matrix interface, particularly at fiber terminations, by quantifying and characterizing the microstructural configuration of a 13wt% CF/ABS polymer composite LAAM printed bead specimen using 3D X-ray μ-CT imaging technique. We develop custom image data post-processing algorithm to extract and analyze measurable μ-CT voxelated density-based grayscale data. The paper further presents simulation results of the hydrostatic flow-field pressure distribution on the surface of a single ellipsoidal rigid particle in simple shear flow colloidal suspension using FEM analysis. The FEA model development is validated by benchmarking results of the ellipsoidal particle's angular velocity and fiber surface pressure with results obtained from well-known Jeffery's Equation [23]. Additionally, simulation results are presented for cylindrical particle shape having hydrodynamically equivalent aspect ratio as the ellipsoidal particle to capture the effect of sharp geometrical singularities on the fibers surface pressure response typically found in actual chopped fiber reinforcements. The FEA simulation results of the fiber surface pressure distribution provide new insight into potential mechanisms that are likely responsible for the experimentally observed microvoid segregation especially at the fiber-tips within the LAAM printed bead specimen.

2 Methodology

2.1 LAAM Printing Process

This study utilized the Baylor Large Area Additive Manufacturing (LAAM) system to 3D print the discontinuous fiber consolidated polymer composite bead. The LAAM system is equipped with a Strangpresse model 19 single-screw extruder (Strangpresse, Youngstown, OH, USA) featuring a nozzle diameter of 3.172 mm with a nozzle height of 1.20mm. The LAAM feedstock material consisted of 13wt% short carbon fiber reinforced ABS (13wt% CF/ABS) pellets purchased from PolyOne (Avient Corporation, Avon Lake, OH, USA). These pellets were dried in a convection oven at 80°C for twelve hours before the 3D printing. A short section of a single bead deposited on the unheated print bed was sampled for this study. The LAAM printing processing conditions includes a temperature of 210°C with a screw extruder speed of 90rpm and nozzle translation speed of 240 cm/min.

2.2 µ-CT Image Data Acquisition Technique

The North Star Imaging X3000 μ CT system (North Star Imaging, Rogers, MN, USA) was employed to scan the CF/ABS sample. μ CT scans were conducted at a resolution of 1.7 microns, utilizing an X-ray source set to 60 kV and 900 μ A to ensure sufficient contrast between the various phases constituting the bead specimen. The sample underwent a full 360-degree rotation in 1-degree increments, resulting in 2400 projections. The detector captured the transmitted X-ray signals, obtaining 2D attenuation distribution data. The acquired μ CT scan data were subsequently reconstructed using efX-CT software (North Star Imaging, Minnesota, USA).

2.3 µ-CT Image Data Post Processing & Analysis

Three dimensional (3D) voxelated density-based grayscale data of a small region of interest (ROI) derived from µCT X-ray image analysis from a cut sample of a 13wt% carbon fiber filled polymer composite bead (cf. Fig. 1) printed with Baylor's LAAM system is analysed using a custom-built post processing code developed in MATLAB (MathWorks, Natick, MA, USA) to obtain volume information of the inherent bead microstructure. The ROI is a cube of dimension 0.25x0.25x0.25mm containing 1.4µm density-based grayscale voxel cubes. Each side length of the ROI has 178 voxels yielding a total of 5,639,752 voxels within the ROI. Feature identification based on binary image segmentation of the ROI volume into the various microconstituent phases including ABS polymer matrix, micro-voids, and fiber phases is achieved by grayscale data thresholding using 'imsegkmeans3' statistical function. The optimized grayscale threshold for the different phases is shown in Fig. 2 below and the resulting segmented microconstituent phases is shown in Fig. 3(a-c). Categorization of individual fibers of fiber clusters and individual micro-void volumes is determined based on voxel connectivity of similar micro-constituent phase using 'bwlabeln' function. Disentanglement of fiber clusters into pristine fibers is achieved by a combination of intensity adjustment and filtering operations with the help of 'imadjustn' and Hessian-based Frangi-Vesselness 'fibermetric' functions. Skeletonization operation is carried out using the 'bwskel' function to extract individual skeletons of the disconnected pristine fibers. The filtering operation preceding skeletonization seldom erodes fiber cluster data, that results in unwanted fragmentation of individual fibers and fiber skeleton. As such, an algorithm that tracks and stitches adjacent fiber fragments along unique orientation paths within reasonable end contiguity tolerance is developed using centroid and orientation region property information of the fiber skeletons obtained with the 'regionprops3' function. Using "bwmorph3" morphological operation function, the endpoints of fibers skeletons are obtained. We define fiber tip regions with 5-voxel unit loci around the fiber skeleton endpoints within the fiber volume.

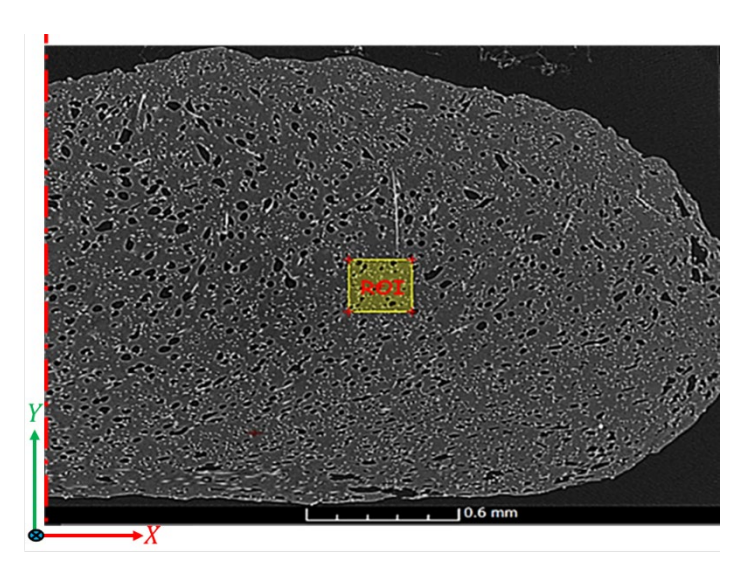


Fig. 1. Showing region of interest (ROI) analyzed from the 13wt% CF/ABS bead specimen.



Fig. 2. Grayscale data threshold ranges for the various phases.

Fig. 4(a) shows the resulting fiber tip regions (green) from the post-processing operation. Important microstructural volume information such as the proportion of void phase in contact with fibers or fiber tip regions is obtained by juxtaposing respective interacting phases of interest through appropriate indexing operation. Fiber tip regions close to the bounding surface of the ROI are excluded from the calculations by defining a buffer zone of 5-voxel units from the ROI edges to account for the probability of the fibers extending beyond the ROI bounds as shown in **Fig. 4**(b). A volume view of the post-processed ROI volume highlighting important microstructural features including the carbon fiber features (gray), voids in contact with fiber tip regions (blue),

voids not in contact with fiber tips (red) can be seen in Fig. 4(b). Fig. 4(c) shows a magnified view of sample fibers (gray) and fiber tip regions (green) and the associated voids touching fiber tips (red).

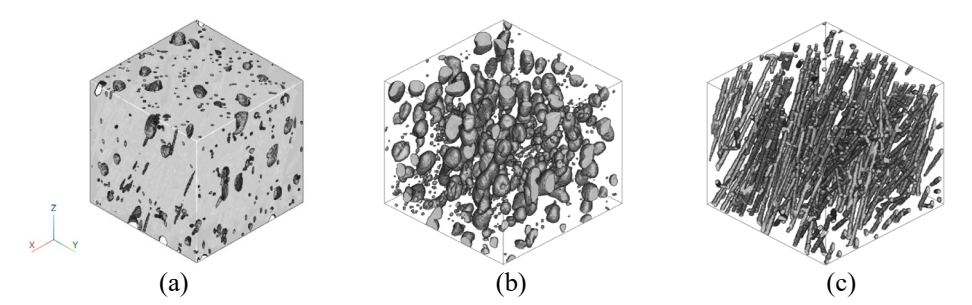


Fig. 3. Segmented microstructural phases: (a) ABS matrix (b) micro-voids (c) fiber consolidation.

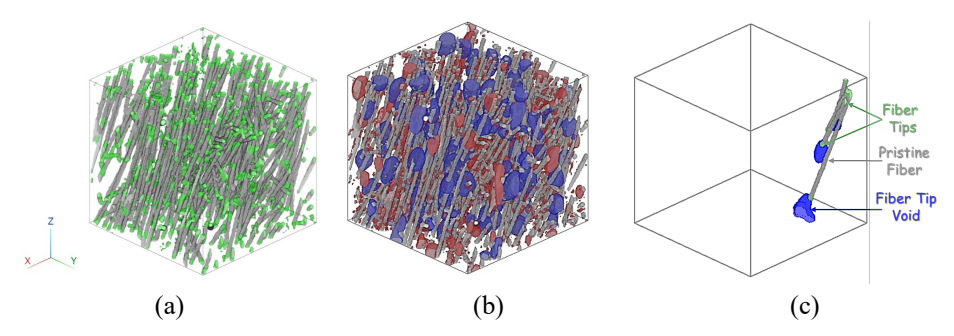


Fig. 4. Showing (a) ROI volume highlighting fiber features (gray), and fiber tip regions (green) (b) ROI volume highlighting fiber features(gray), voids in contact with fiber tips (excluding buffer zone) (blue), and voids not touching fibers (red) (c) Annotated plot detailing the individual microstructural features. (Cubic ROI Size:0.25mm x 0.25mm x 0.25mm)

2.4 Simulating Hydrostatic Flow-Field Pressure

The model formulation of most known void nucleation mechanisms in literature has shown that heterogenous mode micro-void formation during polymer melt processing readily depends on the local flow field pressure distribution [16-22]. Upon satisfaction of some necessary conditions requiring a drop in hydrostatic field pressure below some critical value, voids begin to nucleate [16-22]. The polymer-melt flow through a typical extrusion-deposition additive manufacturing (EDAM) extruder nozzle comprises a combination of uniaxial, shear and rotational flows depending on the nozzle geometry and operating parameters including rheological and viscoelastic properties of the polymer melt, process temperature and pressure [29]. Nozzle flow regimes characterized by exacerbated shear rates have been shown in literature [27] to be the major cause of extreme pressure fluctuations at the tips of fibers which are typical conditions found near the walls of the nozzle where high voids content have

been reported [5]. As such, knowledge of the pressure distribution around the particle's surface can provide useful information into the potential mechanisms that results in void nucleation and segregation at fiber terminations. The dynamics and pressure field surrounding a typical rigid ellipsoidal particle suspended in homogenous, viscous simple shear flow is simulated using a custom finite element analysis code written in MATLAB (MathWorks, Natick, MA, USA). The model development is well documented in [27,30,31]. The governing physics of the fluid flow model are based on Stokes creeping flow equations of mass and momentum conservation considering steady state, incompressible, Newtonian, and isothermal flow conditions with negligible inertia. A non-porous and non-deformable fiber surface with zero slip tolerance is assumed in the model. FEA Galerkin mixed method algorithm is used to transform the strong form equations to weak formulations utilized in the model development. The prescribed essential boundary conditions in the current model are similar to those defined for the single fiber evolution model development presented in [27,30]. As in the usual manner, the far-field velocity prescribed on the fluid boundary surface are extrapolated from the local field velocity gradient of the undisturbed flow. The velocities on the fiber surface are computed from the fibers translational and angular velocities using the equation of rigid body motion. A far-field pressure point constraint corresponding to the instantaneous pressure of the undisturbed flow is imposed on a node of the external fluid boundary surface. For optimized computation, the velocity boundary conditions are defined with respect to the fiber's local coordinate reference axes. The flow domain is discretized using a radial seed of 39 nodes with an average radial bias of 1.2, a polar seed of 18 equally spaced nodes about the major axis of the fiber and an azimuthal seed of 25 nodes along the half the major arc of the ellipsoid with a bias of 1.025 towards the tip (cf. Fig. 5(a&b)). A 10-node quadratic isoparametric serendipity, tetrahedron element (cf. Fig. 5(c)) is used for the simulation with 6 mid-side nodes (i.e. 6 velocities dofs) and 4 vertex nodes (i.e. 4 velocities and pressure dofs) yielding a total of 11286 domain elements. The ratio of the fluid domain radius to half the long fiber axis length is 10 to 1 which is deemed sufficient for the simple shear flow analysis.

The element stiffness matrices and force vectors derived from the transformed mixed method based Galerkin formulations are assembled into a global system stiffness matrix, $\underline{\underline{K}}$ and global load vector, $\underline{\underline{f}}$ consisting of the nodal reaction forces and flow rates [27,30] leading to the linear algebraic systems of equations given as

$$\underline{\underline{K}}\,\underline{\underline{u}} = \underline{\underline{f}} \tag{1}$$

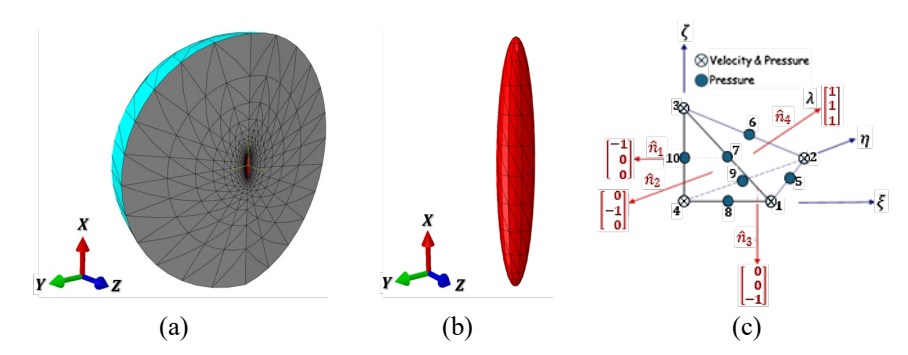


Fig. 5. (a) Fluid domain discretization around the ellipsoidal fiber (b) surface mesh around the walls of the ellipsoidal particle (c) element selection showing active velocity and pressure dofs.

where \underline{u} is the primary variable vector containing nodal velocities and pressures. Partitioning of the system matrix into essential and free degrees of freedom is used to derive solutions of the unknown velocities, pressures, and reactions at the nodes. Newton Raphson's method is used to zero the net hydrodynamic force and torque acting on the fiber's surface to obtain solution of the fiber's translational and angular velocities. The instantaneous fiber translational and rotational velocities are used to update the fiber's position and angle based on an explicit fourth order Runge-Kutta method. More details of the model development can be found in [27]. We validate our FEA model by comparing the results of the evolution of the dimensionless pressure at the particles tip and angular velocity of the particle with the values obtained from Jeffery's analytical formulation [23]. Using similar model assumptions of incompressible, purely viscous, simple shear flow with a Newtonian fluid rheology for particle suspension, Jeffery derived analytical expressions for the particle's in-plane orientation ϕ and angular velocity $\dot{\phi}$ as a function of time given respectively as

$$\phi(t) = \tan^{-1} \left\{ \sqrt{\frac{(1+\xi)}{(1-\xi)}} \tan \left[\frac{\dot{\gamma}}{2} \sqrt{1-\xi^2} t \right] \right\}$$
 (2)

and

$$\dot{\phi}(t) = \frac{\dot{\gamma}}{2} \left[\xi \cos 2\phi + 1 \right] \tag{3}$$

where the particle shape parameter ξ is given as $\xi = (r_e^2 - 1)/(r_e^2 + 1)$. He also derived expression for hydrostatic pressure field surrounding a rigid ellipsoidal particle in viscous suspension given as

$$p = p_0 + 2\mu \left\{ A \frac{\partial^2 \Omega}{\partial x^2} + B \frac{\partial^2 \Omega}{\partial x^2} + C \frac{\partial^2 \Omega}{\partial x^2} + (F + F') \frac{\partial^2 \Omega}{\partial y \partial z} + (G + G') \frac{\partial^2 \Omega}{\partial z \partial x} + (H + H') \frac{\partial^2 \Omega}{\partial x \partial y} \right\} (4)$$

where p_0 is the undisturbed flow field pressure and Ω is the Laplace function defined as

$$\Omega = \int_{\xi}^{\xi_{00}} \left\{ \frac{x^2}{a^2 + \xi} + \frac{y^2}{b^2 + \xi} + \frac{z^2}{c^2 + \xi} - 1 \right\} \frac{d\xi}{\Delta}$$
 (5)

and a, b, and c define the ellipsoid geometry. Expressions for the constants $A, B, C, F, G, H, F', G', H' & \Delta$ are not provided here as they appear in [23]. The resulting pressure distribution on the ellipsoidal particle surface is presented in dimensionless form, \tilde{p} given as

$$\tilde{p} = \frac{p - p_0}{\mu \dot{\gamma}_e} \tag{6}$$

where $\dot{\gamma}_c = \sqrt{2\underline{\Gamma}:\underline{\Gamma}}$ is a scalar magnitude of the deformation rate tensor $\underline{\Gamma}$. Using a

dynamic viscosity of $\mu = 1$ Pa.s, a shear rate, $\dot{\gamma} = 1$ s^{-1} , and an ellipsoidal particle aspect ratio, $r_e = 6$, we present solutions for the evolution of the fibers' angular velocity, $\dot{\phi}$ and fiber surface tip pressure P as a function of the particle in-plane orientation angle, ϕ for both FEA simulation and Jeffery's model as shown in **Fig. 6**(a&b) below. The results show good agreement between the responses obtained from both Jeffery and FEA simulation.

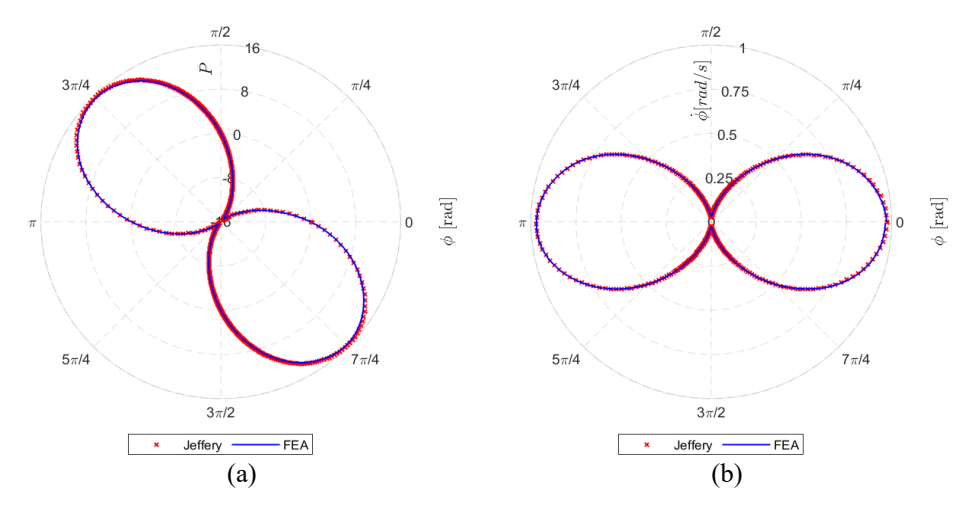


Fig. 6. Evolution of the (a) ellipsoidal particle's surface tip pressure, and (b) fibers angular velocity, obtained from both FEA simulation and Jeffery's analytical calculation.

In reality, the geometry of pristine fiber consolidations present within a typical LAAM composite beads are not ellipsoidal in shape with smooth edges but are better represented by cylindrical particles. Moreover, the chopped ends of the fibers reinforcement do not possess a clearly defined tip as the ellipsoid but are rather characterized by sharp geometrical transitions at the fiber terminations that likely results in pressure singularities. To investigate the existence of exacerbated pressure extremes at the fiber ends, we consider a cylindrical shaped fiber in our FEA simulation choosing a cylindrical aspect ratio that yields the equivalent hydrodynamic ellipsoidal aspect ratio of $r_{\rm g} = 6$. Using approximate formulations develop by Zhang et al [31],

with minor adjustment we derive a cylindrical aspect ratio of $r_e = 7.8$. Unfortunately, besides other drawbacks, Jeffery's model equations are only applicable to ellipsoidal shaped particles and cannot model arbitrary shaped particles, however, our FEA simulation has the advantage of modelling complex particle shapes. Moreover, other deviations from standard Jeffery's assumption can be incorporated in the FEA simulation such as non-Newtonian and visco-elastic fluid rheology, deformable fiber boundaries, etc. We develop a fluid domain mesh using ABAQUS Std. (Simulia ABAQUS, Dassault Systemes SE, Velizy-Villacoublay, France) for the single cylinder suspension using similar fluid domain size ratio, 10 times the cylinder length as shown in Fig. 7(a) below. Mesh refinement zone close the cylinder surface is defined in order to accurately capture the field response on the fibers surface (cf. Fig. 7(b&c)) resulting in a total of 24687 elements. The results of the evolution of the particles angular velocity along Jeffery's orbit for the ellipsoidal particle is benchmarked with that of the cylindrical particle using the same fluid viscosity and shear rate as was previously defined to ensure appropriate equivalent hydrodynamic aspect ratio has been accurately selected. The plots of the particles dynamics and pressure responses are presented in the result section below.

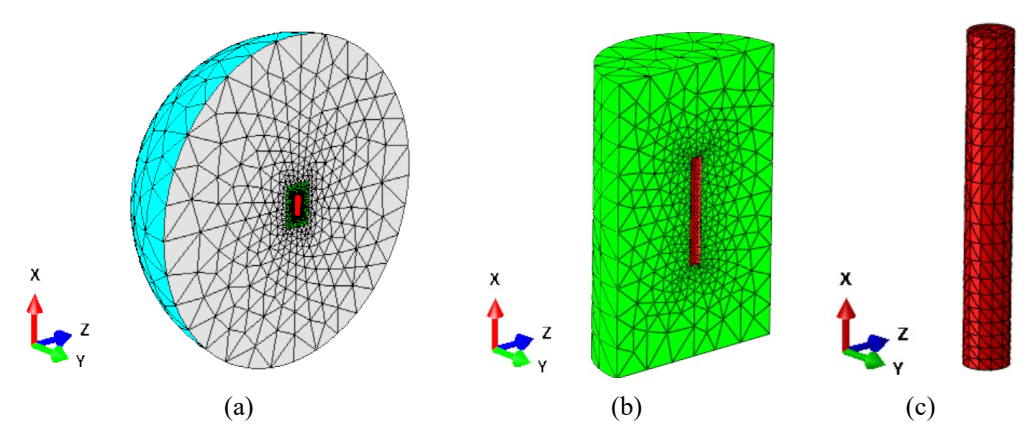


Fig. 7. (a) Fluid domain discretization around the cylindrical fiber (b) mesh refinement zone (c) surface mesh around the walls of the cylindrical particle.

3 Results and Discussion

Microstructural characterization of the ROI volume is carried out based on eight (8) different metrics including the (1) the volume content of the micro-constituent phases including the micro-void phase, ϑ_v , the fiber phase, ϑ_f and ABS matrix, $\vartheta_m = 1 - \vartheta_v - \vartheta_f$, (2) the proportion of voids isolated within the matrix, ϑ_{vm} , (3) the volume fraction of voids in contact with fiber tips, ϑ_{vt} , (4) the average equivalent diameter of voids isolated within the matrix, d_{vm} (5) the average equivalent diameter of voids touching fiber(s), d_{vf} , (6) the average sphericity of the micro-voids isolated within the matrix Φ_{vm} , (7) the average sphericity of micro-voids touching

fibers, Φ_{vf} and (8) the principal components of the region-averaged fiber orientation tensor \mathbf{a}_{ij} . The equivalent void diameter is calculated from a sphere of equal volume as the micro-void feature according to eqn. (7).

$$d_{v} = \sqrt[3]{6/\pi V_{v}}$$
(7)

The micro-void sphericity Φ is computed based on the Wadell definition [32] and given as

$$\Phi = \frac{\sqrt[3]{36\pi V_v^2}}{A_v} \tag{8}$$

where A_v and V_v in eqn. (7) and (8) above are boundary area and volume of individual micro-void features. From **Table 1**, we see the volume fractions of the micro-voids and fiber phases within the extracted ROI region are respectively $\vartheta_v = 11.22\%$ and $\vartheta_f = 6.32\%$. The calculated void content is close to the value obtained from experimental analysis in a separate study by Sayah et al. [33], about 11.68%. Although the manufacturer reported content of the fiber reinforcement within the virgin raw pellets prior to processing is 8.2% by volume, we observe lower fiber contents within the ROI from the extruded bead due to the higher porosity content within this region. Sayah et al. [33] shows that the fiber content varies from as low as 6.5% in bead regions with high void content to about 8.8% where resin lean regions with low void content. The micro-void content isolated within the polymer matrix (i.e. not in contact with fibers) is seen to be very low, $\vartheta_{vm} = 4.91\%$ which implies that more than 95% of the void volume are touching fibers. More importantly, the fraction of void content in contact with fiber tips is seen to be very high, $\vartheta_{vt} = 80.63\%$.

Table 1. Volume content of relevant microstructural features within the ROI volume.

#	Symbol	Units	Description	Value
1(a)	ϑ_v	%	Void volume fraction	11.22
1(b)	ϑ_f	%	Fiber volume fraction	6.32
2	ϑ_{vm}	%	Fraction of voids isolated in matrix	4.91
3	ϑ_{vt}	%	Fraction of voids touching fiber tip(s)	80.63
4	d_{vm}	μm	Average diameter of isolated voids	5.83
5	d_{vf}	μm	Average diameter of interfacial voids	33.72
6	Φ_{vm}	-	Average sphericity of isolated voids	0.67
7	Φ_{vf}	-	Average sphericity of interfacial voids	0.51

The average equivalent diameter of micro-voids isolated within the polymer matrix is seen to be relatively low, $d_{vm} = 5.83 \,\mu m$ compared to the equivalent diameter of the voids touching fibers, $d_{vf} = 33.72 \,\mu m$. Additionally, the calculated sphericity of the voids isolated within the matrix is seen to be relatively higher, $\Phi_{vm} = 0.67$ compared to the average sphericity of voids in contact with fibers, $\Phi_{vf} = 0.51$. By mere visual inspection of the ROI volume information of the different micro-voids categories presented in Fig. 8(a-c) below, the reported values of the micro-void content and characteristics of the analyzed ROI volume in Table 1 above can be easily corrobo-

rated. **Fig. 8**(a) shows the micro-voids isolated within the polymer matrix observed as small-sized dispersed rounded particles compared to the micro-voids touching fibers including those in contact with fiber tips (cf. **Fig. 8**(b)) and those not in contact with fiber tips (cf. **Fig. 8**(c)) which are observed as larger sized irregular agglomerates. Moreover, the content of the micro-voids in contact with fiber tips (cf. **Fig. 8**(b)) is observed to be extremely high compared to micro-void content not touching fiber tips (cf. **Fig. 8**(c)).

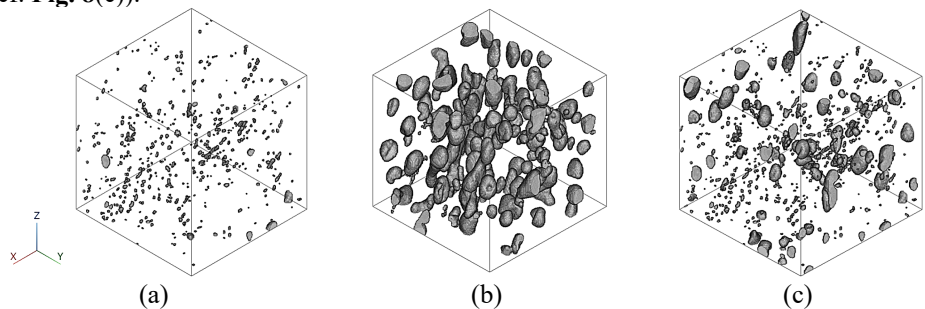


Fig. 8. ROI volume showing (a) micro-void content isolated within the matrix (b) micro-voids content touching fiber tips (c) micro-void content not touching fiber tips.

The region averaged fiber orientation principal components for the ROI volume are presented in **Table 2** below. Reported results shows a very high degree of fiber alignment in the z direction, $a_{zz} = 0.71$ compared to other component directions. The degree of fiber alignment with the print direction (z) across an extruded bead has been shown by Sayah et al. [33] to vary inversely with the micro-void content across the bead.

Table 2. Average values of the fiber orientation principal components within the ROI volume

Symbol	\mathbf{a}_{xx}	a_{yy}	\mathbf{a}_{zz}
Value	0.19	0.10	0.71

The variability in the results of the microstructural analysis of the 13wt% CF/ABS specimen were presented in a more comprehensive statistical study carried out using different and larger sized ROI samples from multiple discrete locations within a bead specimen [34]. As would be expected, there were slight variations in the microconstituents phase contents across the bead regions due to process related factors such as shear rates and cooling rate variability. However, the measured microstructural characteristics such as the average diameter and sphericity were found to be mostly consistent across the bead regions with only minimal variation observed which affirms confidence in our approach. It is worth noting however that with larger ROI volumes, the fraction of voids touching fiber tips are observed to be higher as in [34].

Simulation results of the fibers angular velocity and minimum surface pressure evolution are presented in Fig. 9 below for both cylindrical fiber ($r_c = 7.8$) and equivalent ellipsoidal fiber ($r_e = 6$) to provide insight into the experimentally ob-

served phenomenon of micro-void nucleation at the tips of suspended fibers. The fibers orientation angle, rotational velocity, and surface pressure were computed using flow parameters of $\mu = 1 \, Pa. \, s$, $\dot{\gamma} = 1 \, s^{-1}$. Because the cylindrical fiber has no clearly defined tip, the evolution of the instantaneous minimum surface pressure evolution is reported for both shapes. Fig. 9(a) below shows matching dynamic profile plot for the cylindrical shaped particle and equivalent hydrodynamic ellipsoidal particle which validates accurate determination of the cylindrical aspect ratio. Fig. 9(b) shows the evolution of the minimum pressure on the fiber surface for both shapes. The results show that the fiber surface pressure minimum drops to a minimum value along Jeffery's orbit in both cases. For the ellipsoidal particle, the orbital minimum pressure is seen to occur at a value of P = -15.71 and at orientation angle $\phi = \pi/4$ and $5\pi/4$ radians corresponding to the principal directions of the shear plane flow field. For the cylindrical particle, as expected we observe relatively higher orbital minimum pressure magnitudes of P = -19.7 which occurs further downstream at an angular position $\phi = .917$ and 4.043 radians. The results of the pressure contours (cf. Fig. 9(c&d)) at the location of orbital minimum pressure show that the particle surface pressure minimum occurs at the particle tips at maximum loci from the particle center where the velocity magnitude is always maximum. For the ellipsoidal shaped particle with well-defined tip, Fig. 9(c) clearly shows that the surface minimum pressure would always occur at the tip location however for the cylindrical particle with no clearly defined tip, the location of minimum surface pressure is seen to occur on the flat surface of the cylinder close to its edges (cf. Fig. 9(d)), and the actual position would depend on the relative positioning of the fiber with flow field.

The occurrence of minimum surface localized pressure below the reference global pressure at the tips of suspended fibers from our simulation results elucidates on possible mechanisms that explains the experimentally observed high content of void segregation at the ends of fibers within our LAAM manufactured CF/ABS polymer composite bead. The negative net pressure at the fiber ends in shear dominant flow regimes of the LAAM nozzle may provide favorable sites for micro-void nucleation as we have shown from our $\mu\text{-CT}$ results that a high quantity of micro-voids nucleates at the fiber terminations in our CF/ABS sample bead.

The current study has been conducted using 13wt% CF/ABS polymer composite material. Other materials and processing conditions may likely yield different microstructure characteristics owing to various factors. For instance, polymer materials with higher viscosity are expected to possess higher micro-void contents [10,11]. Moreover, higher fiber content within a particular polymer composite material is expected to yield a higher void content due to increased effective viscosity [10,11]. Additionally, other printing process parameters are expected to result in variations in microstructures as well. For example, while higher extrusion rates and temperature were shown to decrease the void contents in a 13wt% CF/ABS bead [5], higher shear rates and extrusion temperature increased the void content in a 35wt% glass fiber reinforced polystyrene (35wt% GF/PS) composite [10]. In the introduction section, we highlighted properties of a particular polymer composite material such as the average length of fiber reinforcements, sizing agent and coefficient of thermal expan-

sion (CTE) of the fiber and matrix that may further influence the formation of microvoids within the resulting microstructure. The mechanism of micro-void nucleation at the tips of suspended particles is seen irrespective of the material selection or process conditions which is seen in our current investigation with 13wt% CF/ABS composite and in previous studies on 20wt% GF/Noryl extrudates [10].

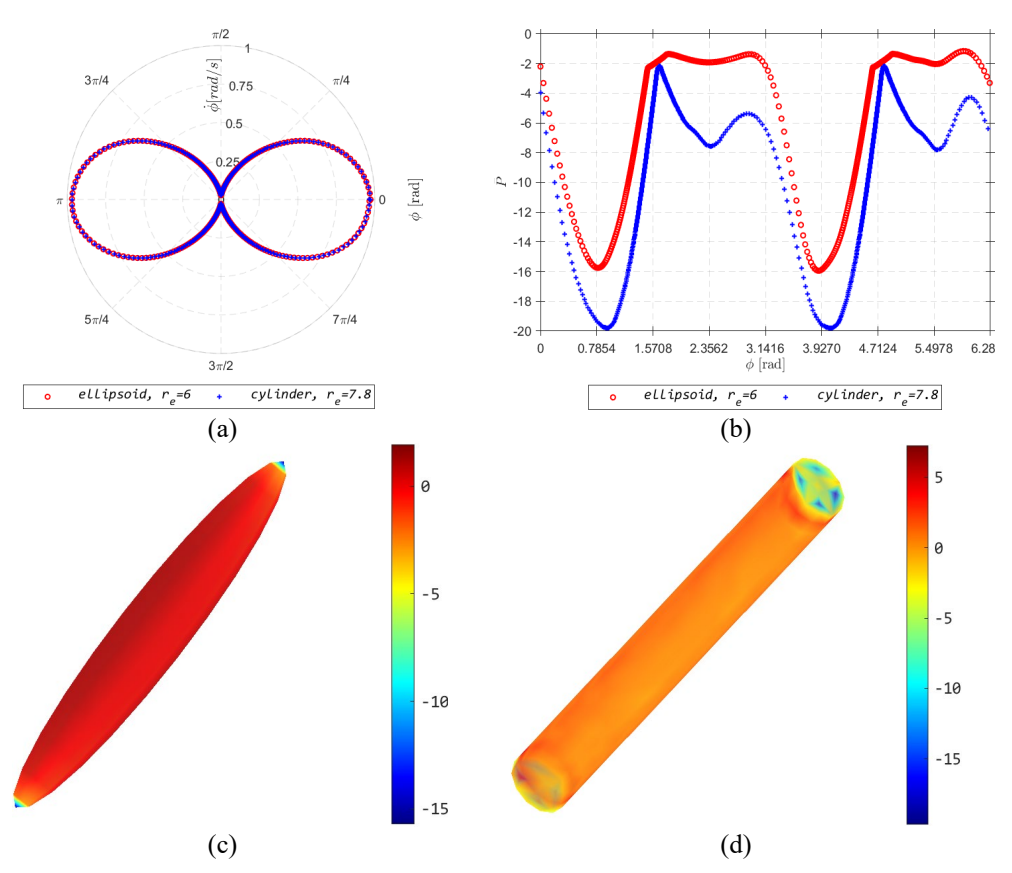


Fig. 9. Evolution of the (a) fibers angular velocity, (b) fiber's minimum surface pressure (along Jeffery's orbit) for ellipsoidal particle shape (red) and cylindrical particle shape (blue). Distribution of the fibers surface non-dimensionless pressure at the location of minimum orbital pressure for (c) ellipsoidal particle ($\phi = \pi/4$) and (d) cylindrical particle ($\phi = .917$).

4 Conclusion

In summation, microstructural characterization of a 13wt% CF/ABS bead specimen printed from Baylor's LAAM system using X-ray μ -CT imaging was carried out in particular to determine the content of the micro-constituent phases present (ABS, micro-voids, fibers) and evaluate the fractions of different categories of micro-voids,

their average size and sphericity together with the average fiber orientation. We find that most of the heterogenous mode micro-voids are segregated at the fiber terminations. Micro-voids that formed at the fiber-matrix interface were observed to be larger and more irregular in shape compared to the homogenous mode micro-voids isolated within the polymer matrix which were much smaller in size and more rounded in shape. The FEA simulation results were used to provide insight into underlying mechanisms likely responsible for heterogenous mode micro-void nucleation at the fiber-matrix interface. Model validation carried out by comparing results of dynamics and surface pressure distribution of a single rigid ellipsoidal particle suspended in homogenous, Newtonian simple shear flow showed that the FEA results matched result obtained from Jeffery's model. The FEA simulation results also showed the particles surface pressure distribution is minimum at the tip locations and this localized minimum pressure drops well below the global reference value during the particles motion along Jeffery's orbit. Simulation result of the cylindrical shaped particle having hydrodynamically equivalent ellipsoidal aspect ratio revealed much higher surface pressure extreme magnitudes at the geometric singularities of the fibers surface. The occurrence of very low negative surface pressure at the tips of fibers helps shed light into potential cause of the high fraction of micro-voids experimentally observed to nucleate at fiber tips. A future direction in the simulation effort would capture effects typically found in the actual structure of the fiber suspension such as the actual fiber geometry imported from the µ-CT data, the inter- and intra-particle hydrodynamic forces, the shear-thinning fluid rheology, and Brownian effects etc. which all potentially affect the resulting pressure distribution on the fibers surface. Based on the proposed micro-void nucleation mechanism, a potential way for mitigating their formation would leverage factors that reduce the pressure intensity at the fibers tip such as proper fiber surface finishing that reduce sharp tip curvatures, selecting a lower viscosity polymer matrix material and optimizing the printing parameters.

Acknowledgement. The authors wish to acknowledge the National Science Foundation for providing the necessary grants that made this publication possible. We would also like to thank Strangpresse for donating the Model 19 single screw extruder that enabled us to study LAAM extrusion deposition of polymer composite materials in Baylor's Laboratory.

References

- 1. Hmeidat, N.S., Elkins, D.S., Peter, H.R., Kumar, V. and Compton, B.G., 2021. Processing and mechanical characterization of short carbon fiber-reinforced epoxy composites for material extrusion additive manufacturing. Composites Part B: Engineering, 223, p.109122.
- 2. Fu, S.Y., Lauke, B., Mäder, E., Yue, C.Y. and Hu, X.J.C.P.A.A.S., 2000. Tensile properties of short-glass-fiber-and short-carbon-fiber-reinforced polypropylene composites. Composites Part A: Applied Science and Manufacturing, 31(10), pp.1117-1125.
- 3. Fu, S.Y. and Lauke, B., 1996. Effects of fiber length and fiber orientation distributions on the tensile strength of short-fiber-reinforced polymers. Composites Science and Technology, 56(10), pp.1179-1190.
- 4. Brenken, B., Barocio, E., Favaloro, A., Kunc, V. and Pipes, R.B., 2018. Fused filament fabrication of fiber-reinforced polymers: A review. Additive Manufacturing, 21, pp.1-16.

- Sayah, N. and Smith, D.E., 2022. Effect of Process Parameters on Void Distribution, Volume Fraction, and Sphericity within the Bead Microstructure of Large-Area Additive Manufacturing Polymer Composites. Polymers, 14(23), p.5107.
- Sommacal, S., Matschinski, A., Drechsler, K. and Compston, P., 2021. Characterisation of void and fiber distribution in 3D printed carbon-fiber/PEEK using X-ray computed tomography. Composites Part A: Applied Science and Manufacturing, 149, p.106487.
- Fallon, J.J., McKnight, S.H. and Bortner, M.J., 2019. Highly loaded fiber filled polymers for material extrusion: A review of current understanding. Additive Manufacturing, 30, p.100810.
- 8. Tekinalp, H.L., Kunc, V., Velez-Garcia, G.M., Duty, C.E., Love, L.J., Naskar, A.K., Blue, C.A. and Ozcan, S., 2014. Highly oriented carbon fiber–polymer composites via additive manufacturing. Composites Science and Technology, 105, pp.144-150.
- 9. Papon, E.A. and Haque, A., 2020. Review on process model, structure-property relationship of composites and future needs in fused filament fabrication. *Journal of Reinforced Plastics and Composites*, 39(19-20), pp.758-789.
- Vaxman, A., Narkis, M., Siegmann, A. and Kenig, S., 1989. Void formation in short-fiber thermoplastic composites. *Polymer Composites*, 10(6), pp.449-453.
- Narkis, M., Vaxman, A., Kenig, S. and Siegmann, A., 1989. Quantitative measurement of fiber orientation and fracture, void and weld-lines in short fiber reinforced thermoplastic composites. *Journal of Thermoplastic Composite Materials*, 2(4), pp.307-318.
- Eom Y, Boogh L, Michaud V, Sunderland P, Månson JA. Stress-initiated void formation during cure of a three-dimensionally constrained thermoset resin. *Polymer Engineering & Science*. 2001 Mar;41(3):492-503.
- Yang, D., Zhang, H., Wu, J. and McCarthy, E.D., 2021. Fiber flow and void formation in 3D printing of short-fiber reinforced thermoplastic composites: An experimental benchmark exercise. *Additive Manufacturing*, 37, p.101686.
- Yu, S., Bale, H., Park, S., Hwang, J.Y. and Hong, S.H., 2021. Anisotropic microstructure dependent mechanical behavior of 3D-printed basalt fiber-reinforced thermoplastic composites. *Composites Part B: Engineering*, 224, p.109184.
- Ning, F., Cong, W., Qiu, J., Wei, J. and Wang, S., 2015. Additive manufacturing of carbon fiber reinforced thermoplastic composites using fused deposition modeling. Composites Part B: Engineering, 80, pp.369-378.
- Titomanlio, G., Piccarolo, S. and Marrucci, G., 1985. Analysis of void formation in extruded bars. *Polymer Engineering & Science*, 25(2), pp.91-97.
- 17. Titomanlio, G., Piccarolo, S. And Marrucci, G., 1987. Non-Newtonian analysis of void formation in extruded polymeric bars. *Chemical Engineering Communications*, 53(1-6), pp.49-59.
- Roychowdhury, S., Gillespie Jr, J.W. and Advani, S.G., 2001. Volatile-induced void formation in amorphous thermoplastic polymeric materials: I. Modeling and parametric studies. *Journal of Composite Materials*, 35(4), pp.340-366.
- 19. Han, J.H. and Dae Han, C., 1990. Bubble nucleation in polymeric liquids. II. Theoretical considerations. *Journal of Polymer Science Part B: Polymer Physics*, 28(5), pp.743-761.
- 20. Stewart, C.W., 1970. Nucleation and growth of bubbles in elastomers. Journal of Polymer Science Part A-2: Polymer Physics, 8(6), pp.937-955.
- 21. Han, J.H.P., 1988. Bubble nucleation in polymeric liquids. (Doctoral dissertation, Polytechnic Institute of NewYork).
- Colton, J.S. and Suh, N., 1987. The nucleation of microcellular thermoplastic foam with additives: Part I: Theoretical considerations. *Polymer Engineering & Science*, 27(7), pp.485-492.

- 23. Jeffery, G. B. The motion of ellipsoidal particles immersed in a viscous fluid. *Proceedings of the Royal Society of London. Series A*, 102(715):161-179, 1922.
- Abtahi, S.A. and Elfring, G.J., 2019. Jeffery orbits in shear-thinning fluids. *Physics of Fluids*, 31(10), p.103106.
- 25. Zhang, D. and Smith, D.E., 2015. Finite element-based brownian dynamics simulation of nanofiber suspensions using Monte Carlo Method. *Journal of Micro and Nano-Manufacturing*, 3(4).
- 26. Férec, J., Bertevas, E., Khoo, B.C., Ausias, G. and Phan-Thien, N., 2021. Rigid fiber motion in slightly non-Newtonian viscoelastic fluids. Physics of Fluids, 33(10).
- Awenlimobor, A., Smith, D.E. and Wang, Z., 2024. Simulation of fiber-induced melt pressure fluctuations within large scale polymer composite deposition beads. *Additive Manufacturing*, 80, p.103980.
- Garcea, S.C.; Wang, Y.; Withers, P.J. X-ray computed tomography of polymer composites. Compos. Sci. Technol. 2018, 156, 305–319.
- Schuller, T., Fanzio, P. and Galindo-Rosales, F.J., 2023. The impact of polymer rheology on the extrusion flow in fused filament fabrication. arXiv preprint arXiv:2311.05158.
- Awenlimobor, A., Wang, Z. and Smith, D.E., 2021. Physical Modeling: Simulation of Micro-Void Development within Large Scale Polymer Composite Deposition Beads. In 2021 International Solid Freeform Fabrication Symposium. University of Texas at Austin.
- 31. Zhang, D., 2013. Flow-Induced Micro-and Nano-Fiber Suspensions in Short-Fiber Reinforced Composite Materials Processing. (Doctoral Dissertation, University of Missouri-Columbia).
- 32. Wadell, H., 1935. Volume, shape, and roundness of quartz particles. The Journal of Geology, 43(3), pp.250-280.
- 33. Sayah, N. and Smith, D.E., 2024. Correlation of Microstructural Features within Short Carbon Fiber/ABS Manufactured via Large-Area Additive-Manufacturing Beads. Journal of Composites Science, 8(7), p.246.
- 34. Awenlimobor, A., Sayah, N. and Smith, D.E., 2024. Micro-void nucleation at fiber-tips within the microstructure of additively manufactured polymer composites bead. *Composites Part A: Applied Science and Manufacturing*, p.108629.